



Mechanical testing and macro-mechanical finite element simulation of the deformation, fracture, and short circuit initiation of cylindrical Lithium ion battery cells

Lars Greve^{a,*}, Clemens Fehrenbach^{b,1}

^a Volkswagen AG, Group Research, Letter box 1777, D-38436 Wolfsburg, Germany

^b Fraunhofer Institute for Mechanics of Materials IWM, Woehlerstr. 11, D-79108 Freiburg, Germany

HIGHLIGHTS

- ▶ Mechanical cell testing with in-situ short circuit location identification.
- ▶ Macroscopic jelly roll fracture initiates the internal short circuits.
- ▶ Stress-based fracture and short circuit criterion developed.
- ▶ Finite element crash simulation of the cell tests.

ARTICLE INFO

Article history:

Received 7 March 2012

Received in revised form

20 April 2012

Accepted 22 April 2012

Available online 28 April 2012

Keywords:

Mechanical

Abuse

Short circuit

Simulation

Fracture

ABSTRACT

A quasi-static mechanical abuse test program on cylindrical Lithium ion battery cells has been performed at a state of charge (SoC) of 0%. The investigated load cases involved radial crushing, local lateral indentation and global three-point bending of the cell. During the tests, the punch load, the punch displacement, the cell voltage and the temperature development of the cell have been monitored using an infrared camera and temperature sensors. After the test, the cells have been analysed using computer tomography.

It is indicated that macroscopic jelly roll fracture on a global scale initiates the internal short circuits, revealed by a sudden decrease of the global mechanical load due to the rupture, followed by a drop of the measured voltage and immediate increase in cell temperature.

A macro-mechanical finite element crash simulation model has been established for the cell housing and the jelly roll. The classical stress-based criterion after Mohr and Coulomb (MC) has been applied to predict fracture and the initiation of an internal short circuit of the jelly roll. The MC criterion correctly represents the punch displacement to fracture, where the predicted fracture locations correspond to the observed locations of the internal short circuits of the cells.

© 2012 Elsevier B.V. All rights reserved.

1. Introduction

Plug-in hybrid electronic vehicles (PHEV), range extender battery electronic vehicles (RE BEV) and pure battery electric vehicles (BEV) are likely to play an important role in future road traffic, depending on the predicted future regulation scenarios [1].

Currently, the Lithium ion battery technology is of primary interest to the automotive industry, since it provides one of the best energy densities available today, e.g. ([2,3]).

The active material of standard Lithium ion battery cells is represented by stacked or wrapped layers of the cathode and anode material sheets, which are physically separated by a porous but mechanically robust separator foil, in order to help prevent an internal short circuit of the cell. Battery systems in electric vehicles are protected against deformation by massive structural measures in order to fulfil federal crash laws, consumer crash tests and other requirements. Despite these achievements, the knowledge of the limiting deformability of Lithium ion cells prior to short circuit

* Corresponding author. Tel.: +49 5361 9 46562; fax: +49 5361 9 31549.

E-mail addresses: Lars.Greve@Volkswagen.de (L. Greve), clemens.fehrenbach@iwm.fraunhofer.de (C. Fehrenbach).

¹ Tel.: +49 761 5142 151; fax: +49 761 5142 510.

initiation can potentially provide valuable additional information for the design of future battery cells.

On the experimental side, extensive research focused on the investigation of the different cell components, where special emphasis is put on the development and characterisation of separators for improved cell performance ([4–6]).

Simulation-based research included stress and damage analysis due to thermal expansion mismatch of the different electrode components during charging/discharging. Xiao et al. [7] modelled the stress and deformation in electrode particles and separators using a meso-scale representative volume element (RVE) coupled to a 1D macroscopic battery model. Zhang et al. [8] simulated the intercalation-induced 3D stress in Lithium ion battery electrode particles of different size and shape. They concluded that smaller sized particles with large aspect ratios lead to reduced intercalation-induced stresses and damage.

Extensive research also went into the analysis and simulation of abuse tests (oven, short circuit, overcharge, nail, crush), with emphasis on the cell behaviour after short circuit initiation. A summary paper is provided by Spotnitz and Franklin [9]. Maleki and Howard [10] investigated the internal short circuit behaviour of prismatic cells, subject to small nail penetration, small indentation and cell pinching, experimentally and numerically. They concluded that the risk of a critical thermal runaway of the cell is mainly controlled by the local heat conduction of the cell structure around the shorted region. In the worst case of the investigated load cases, namely cell pinching, the heat cannot be transferred to the cell-can, but is transferred back into the jelly roll. Spotnitz et al. [11] simulated the thermal abuse resistance of 18 650-size cells. Analogous to Maleki and Howard [10], the authors identified heat transfer as the governing factor for thermal runaway, where thermal runaway of a single cell of a battery pack is more likely to cause thermal runaway of the whole battery pack when the initiating cell is in good contact with other cells and is close to the pack wall.

Safety issues related to Lithium ion battery cells are discussed controversially in the literature. Generally, there are two different strategies.

1. Improving the safety by avoiding abuse and protecting the cells appropriately.
2. Improving the safety of the cells by understanding the mechanisms causing internal short circuits under mechanical loading, and by improving the cells or cell components accordingly.

Farrington [12] suggested that “effective regulations should promote and maximize safe transportation of lithium batteries through [...] the elimination of unsafe circumstances”. Sahraei et al. [13] believe that “advanced constitutive models are needed for strength/weight optimization and safety assessments of Li-ion

batteries”. The authors performed a comprehensive structural testing program on prismatic pouch cells with the aim to set up a finite element model for representing the deformation behaviour of the interacting cell components on a macro-mechanical homogenized scale, and also on a refined meso-mechanical scale, where individual layers of the electrodes are modelled distinctively. In another paper [14], the same authors investigated cylindrical cells subject to axial crushing, radial crushing (without end caps) and radial indentation, and used numerical finite element simulations and analytical solutions for describing the deformation response of the cells.

The two papers by Sahraei et al. ([13,14]) were the only publications in the open literature found by the present authors in which the deformation behaviour of battery cells during mechanical abuse loading was investigated and modelled. No publications could be identified for predicting the onset of short circuits of battery cells under mechanically loading, using finite element modelling.

In the present study, cylindrical Lithium ion cells are subjected to various mechanical abuse tests, in order to create a crash simulation model of the cell. The developed simulation model allows representation of the cell deformation, and also features a stress-based fracture criterion for predicting the load state and location for internal short circuit onset during deformation.

2. Mechanical cell abuse testing program

2.1. Test preparation

Cylindrical Nickel Cobalt Oxide (NCA) Lithium ion cells (GAIA, HP 602030 NCA-45 Ah/162 Wh) are used in this study. The main cell dimensions are provided in Fig. 1a, and the interested reader is referred to the online data sheet of the cell [15] for further information about the physical and mechanical characteristics, the electro-chemical characteristics, and the operating conditions of the cell.

The cells are discharged at a state of charge (SoC) of slightly greater than 0%, or to the recommended voltage limit for discharge, approximately 3 V, respectively.

A zero SoC is expected to enable assessment of the heat location and propagation at internal short circuit initiation, but at the same time allows avoiding severe cell reaction like smoke and fire development. Three temperature sensors are applied on the cell mandrel, Fig. 1a, and the cell voltage is also recorded during the test.

For safety reasons, the cells are located in a windowed cave featuring a gas exhaust device, Fig. 1b.

The cave is mounted on a hydraulic tension/compression testing device allowing the application of compressive loading using different types of punches and bearings, Fig. 1c. The tests are performed under quasi-static loading at 0.1 mm s^{-1} . During

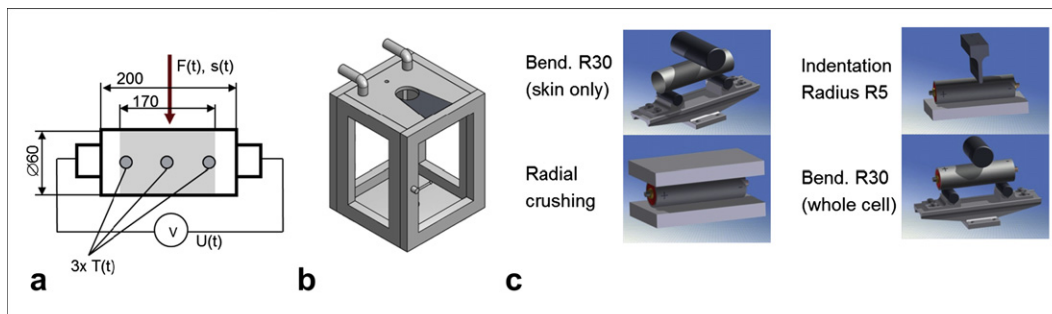


Fig. 1. a) Main cell dimensions (in mm) and cell instrumentation; b) test chamber set up; c) investigated load cases.

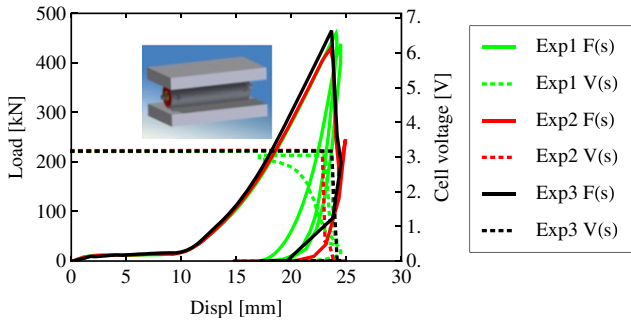


Fig. 2. Experimentally obtained punch load–displacement and cell voltage curves for the load case “radial crushing” of the whole cell.

the test, the load and machine cross head movement are recorded. An infrared camera captures the front view of the cell during the test. The mechanical test was interrupted, once the cell voltage dropped to zero, indicating a potential internal short circuit. At this state, the punch was removed from the cell, and the temperature development of the cell was monitored another hour after the test, in order to prove the occurrence of an internal short circuit. Each load case configuration has been repeated at least two times.

2.2. Test analysis

The load–displacement curves and the cell voltage measurements are provided in Figs. 2–4. It is noted that the cells could endure significant deformation prior to the occurrence of an internal short circuit. A good repeatability of the load–displacement curves and of the punch displacement, at which the cell voltage drops significantly, is observed. In some cases the cell voltage did not immediately decrease to zero, but remained at a reduced level. In these cases, the unloaded punch has been applied again and driven further until the voltage signal decreased to zero, Fig. 2: Exp1. In one of the bending tests, undesired movement of the clamped bearings has been observed, Fig. 4: Exp3.

For all tests, the temperature sensors recorded an increasing temperature from about 25 °C to approximately 50 °C after the tests, proving the occurrence of an internal short circuit. Additionally, the infrared camera recorded high temperature spots at the beginning of the short circuit (cell voltage drop), Fig. 14 in Section 3.5, revealing the location of the short circuit. This crucial information is used as a quality check of the numerical short circuit criterion developed in Section 3.5.

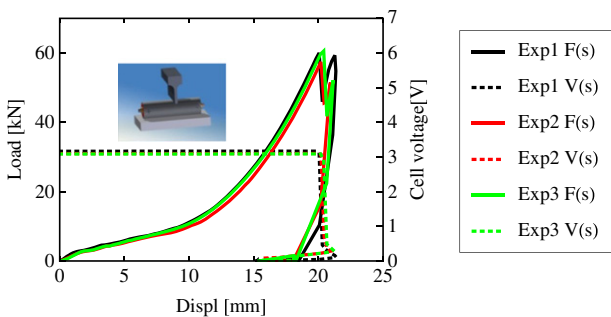


Fig. 3. Experimentally obtained punch load–displacement and cell voltage curves for the load case “indentation” of the whole cell.

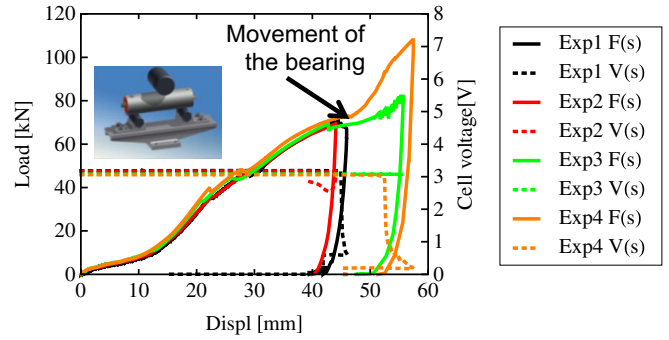


Fig. 4. Experimentally obtained punch load–displacement and cell voltage curves for the load case “bending” of the whole cell.

Interestingly, a sudden drop in the force level is observed in some of the load–displacement curves, just before initiation of the internal short circuit. The effect is most pronounced for the load case “indentation”, Fig. 3. The steel housing did not show any sign of fracture. Hence, it is assumed that the load drop is caused by structural fracture within the jelly roll. A computer tomography (CT) analysis of the cell subjected to bending loading indeed revealed a macroscopic fracture of the jelly roll, Fig. 5. It is interesting to recapitulate that the onset of the short circuit is not just due to fracture phenomena of the separator on a micro- or meso-scale. Macroscopic through-thickness fracture of the jelly roll enables relative movement of the “unprotected” anode and cathode material at the fracture surface, which then easily can lead to direct physical contact of the anode and cathode, or to bridging contact via the steel housing, initiating the short circuit.

For the other load cases, where the zone of internal short circuit is subject to compressive/shear loading, no such clear statement can be made regarding the existence of a macroscopic fracture. It is however likely that existing cracks become closed due to the compressive state of loading, and hence are difficult to detect.

In the next section, a numerical short circuit detection criterion is developed, based on the assumption that fracture within the jelly roll initiates the short circuit.

3. Deformation and fracture modelling of the cell

3.1. Preparation of the simulation model

The commercial explicit crash code Virtual Performance Solution (VPS) is used for the numerical analysis. An overview of the finite element model of the cell, punches and bearings is provided in Fig. 6.

The jelly roll is secured by a 1 mm thick cylindrical stainless steel housing. The housing is represented by shell elements

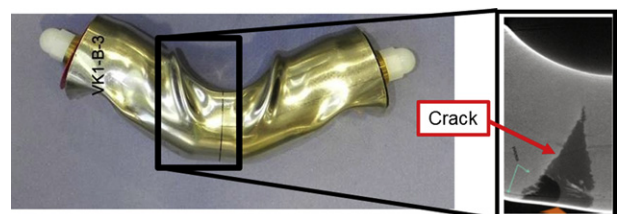
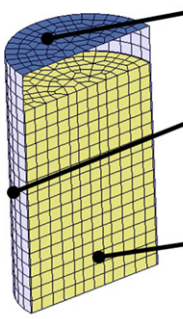


Fig. 5. Deformed cell and computer tomography for the load case “bending”.



Component	Thickness	Material	Plasticity model	Remarks
Cap	0.2 mm	Stainless steel	Isotropic J2 yield criterion	No influence on simulation results; just included for optical reasons.
Outer skin	1.0 mm	Stainless steel	Hill48 yield criterion with normal anisotropy	Shell elements with 5 through-thickness integration points
Jelly roll	-	Nickel Cobalt Oxide (NCO) electro-chemistry	Pressure-dependent isotropic Raghava yield criterion with non-associated flow rule	Central hole and pole connections are neglected.

Fig. 6. Macro-mechanical finite element model of the cell (using quarter model due to symmetry conditions).

(approximately $5 \times 5 \text{ mm}^2$), whereas the jelly roll is represented by volume elements (approximately $5 \times 5 \times 5 \text{ mm}^3$). The inner hole of the jelly roll is neglected in the simulation model, as well as discretization of the pole connectors on each end of the jelly roll. The bearings and the punches are modelled as rigid bodies. A penalty-spring based contact definition is applied between housing and jelly roll, assuming a Coulomb friction coefficient of 0.1. Another contact is applied between the punch, the cell housing and the bearings, using a friction coefficient of 0.1.

The explicit simulations were performed using a time step of one micro-second, which corresponds to a typical value used for full scale vehicle crash simulations. The density of the jelly roll was then trimmed in order to represent the real cell weight of 1.5 kg in the simulation run. The punch intrusion velocity was set to a significantly higher value ($v_{\text{sim}} = 0.5 \text{ mm ms}^{-1}$) than the actual test speed ($v_{\text{exp}} = 0.1 \text{ mm s}^{-1}$), in order to reduce the computation time. At any time during the simulation, the difference of punch force and bearings force was less than 0.2 kN (0.04% of the maximum load), indicating that existing mass inertia forces in the simulation are still negligible in the simulated configuration. All material models used in the subsequent sections are rate independent, so that the increased simulation speed does not influence the model behaviour at all.

3.2. Identification of material model parameters for the housing

Within Volkswagen Group Research, a modular user material model (MMM) for the crash simulation of deformation and fracture of automotive materials has been developed in the past. The

material model is based on a modular concept, where the user can plug-in different modules for elasticity, yield criterion, hardening, fracture and damaging, as required for the given material of investigation. In this study, MMM is used for the simulation of all cell components.

Tensile specimens are cut from flattened housing sheets, Fig. 7. The tensile tests were performed on an electromechanical tensile machine at 0.01 mm s^{-1} , where the load and the local displacement within the gauge section were recorded during the test. Textbook values are used for the Young's modulus, $E_{\text{housing}} = 207 \text{ GPa}$ and the elastic Poisson ratio, $\nu = 0.3$.

The tensile tests revealed a normal anisotropy of the housing sheet, $r = 0.64$, which is represented by the classical Hill48 yield criterion [16]. The strain hardening could be well represented by the modified Swift law [17], as a function of the equivalent plastic strain $\bar{\epsilon}^p$,

$$R_{\text{housing}}(\bar{\epsilon}^p) = k(\epsilon_0 + \bar{\epsilon}^p)^n, \quad (1)$$

with $k = 0.7 \text{ GPa}$, $\epsilon_0 = 0.00801$ and the hardening exponent $n = 0.1385$, Fig. 7b.

A three-point tube bending test is performed for validation of the identified material model parameters of the housing, showing very good agreement of the simulation and experiment, Fig. 8.

3.3. Constitutive model for the jelly roll

The jelly roll is represented by a wrapped stacked sequence of separator, anode, separator and cathode foils, Fig. 9a and b. The

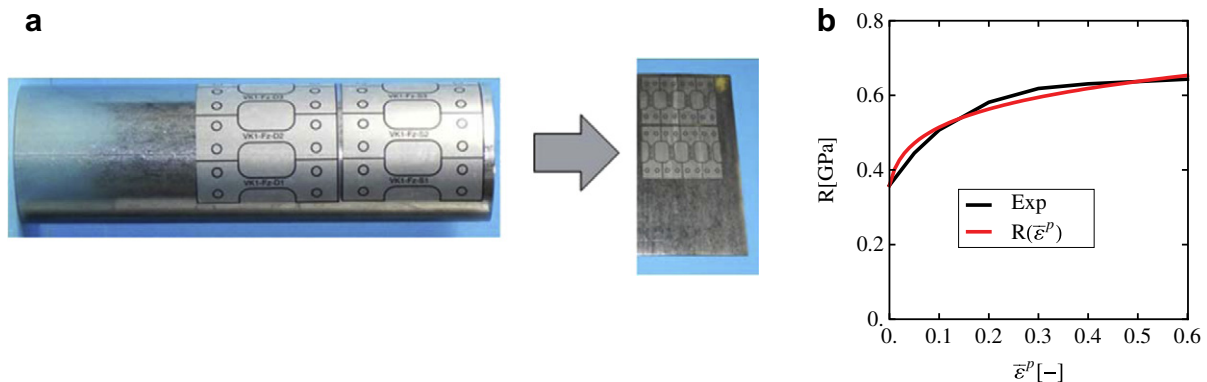


Fig. 7. a) Specimen extraction from the flattened housing tube; b) experimental and analytical hardening curve.

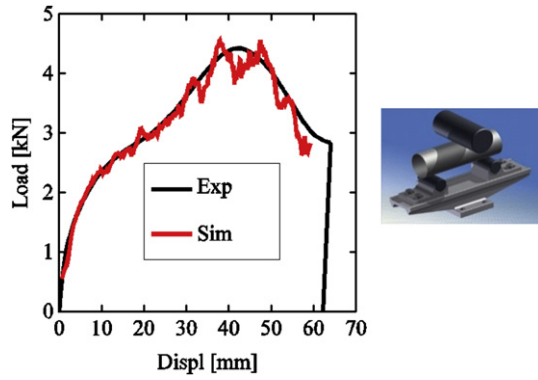


Fig. 8. Three-point bending test of cylindrical housing tube: comparison of experimental and simulated load–displacement curves.

anode material (LiCoO₂ powder) is baked onto the surfaces of the Aluminium current collector, whereas the cathode material features a central Copper foil current collector with a graphite powder coating, Fig. 9b. Both electrode coating materials are highly porous, and soaked in electrolyte fluid. A detailed numerical analysis would require a comprehensive characterisation of all jelly roll components (cathode, anode, separator and foils), and their interaction, e.g. friction and inter-laminar slip. Since the thickness of a separator foil is typically about 0.03 mm, a full 3D finite element representation of the unit cell would require finite elements featuring an element length of similar geometrical size, eventually leading to an unmanageable number of finite elements and computational requirements for industrial crash simulation application. Hence, in this study a simplified macro-mechanical approach is applied, in which the jelly roll is considered isotropic, Fig. 9c. That is, the deformation of the electrodes together with the separator is treated in an integrated and continuous way. The influence of frictional slip between the foils and the influence of potential foil separation (gaping) is neglected.

During compressive mechanical testing, the electrolyte is squeezed out of the porous electrodes, and moves into the empty cavitation at the ends of the cells, so the porous electrodes become compressed and change their circumscribing volume. For phenomenological modelling of the electrode compressibility, a pressure dependent yield criterion, and a pressure dependent non-associated flow rule are proposed. In the following procedure, a generalized plasticity model for the jelly roll components will be proposed. Then, the generalized model will be simplified for the present isotropic modelling approach according to Fig. 9c. The yield criterion reads:

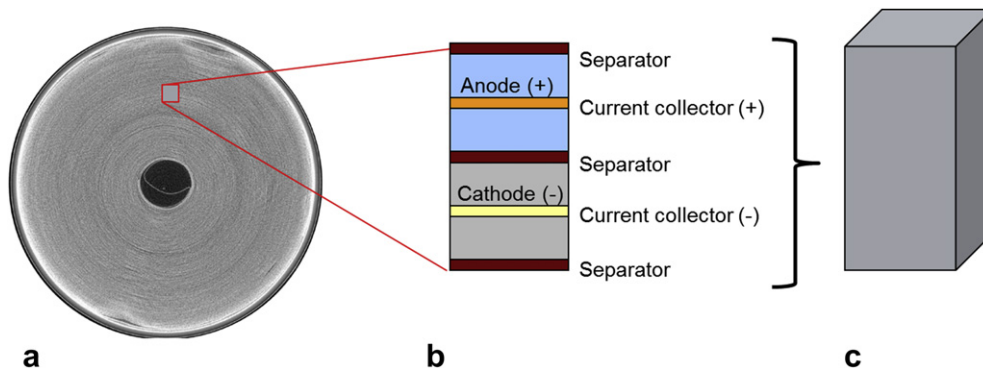


Fig. 9. a) Cross section of the jelly roll; b) unit cell of the jelly roll components; c) simplified isotropic continuum representation of the jelly roll material.

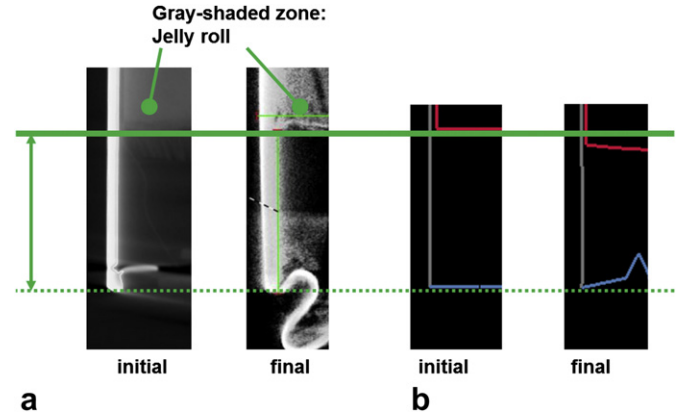


Fig. 10. Analysis of the axial jelly roll deformation at the initial and final state: a) CT analysis; b) jelly roll deformation obtained by simulation.

$$f = \bar{\sigma} - R_{\text{jellyroll}}(\bar{\epsilon}^p) = 0. \quad (2)$$

where $R_{\text{jellyroll}}$ is the hardening function of the jelly roll, and $\bar{\sigma}$ is the equivalent stress, represented by a modified Raghava yield criterion [18]:

$$\bar{\sigma} = \frac{1}{2\alpha} \left(3(\alpha - 1)\sigma_m + \sqrt{9(\alpha - 1)^2\sigma_m^2 + 4\alpha \bar{\sigma}_{\text{dev}}^2} \right), \quad (3)$$

in which the original von Mises equivalent stress is replaced by a generalized anisotropic deviatoric equivalent stress $\bar{\sigma}_{\text{dev}}$.

In equation (3), α represents the absolute ratio of uniaxial compressive and uniaxial tensile yield strength of the material, and σ_m is the hydrostatic stress,

$$\sigma_m = \frac{1}{3}(\sigma_1 + \sigma_2 + \sigma_3), \quad (4)$$

where σ_i are the principal stresses. $\bar{\sigma}_{\text{dev}}$ represents an anisotropic quadratic yield criterion, obtained by linear transformation of the stress vector,

$$\bar{\sigma}_{\text{dev}} = \frac{1}{2}[\mathbf{P}(\boldsymbol{\sigma} - \mathbf{b})]^T(\boldsymbol{\sigma} - \mathbf{b}), \quad (5)$$

where \mathbf{P} is the linear transformation matrix, $\boldsymbol{\sigma} = [\sigma_{11} \ \sigma_{22} \ \sigma_{33} \ \sigma_{12} \ \sigma_{23} \ \sigma_{13}]^T$ is the stress vector, and $\mathbf{b} = [b_{11} \ b_{22} \ b_{33} \ 0 \ 0 \ 0]^T$ is the initial back stress vector.

With an appropriate choice of the matrix components of \mathbf{P} , the deviatoric equivalent stress represents the classical Hill48 yield criterion with an initial back stress vector,

$$\bar{\sigma}_{\text{dev}} = \sqrt{F(\sigma_{22b} - \sigma_{33b})^2 + G(\sigma_{33b} - \sigma_{11b})^2 + H(\sigma_{11b} - \sigma_{22b})^2 + 2[L(\sigma_{23})^2 + M(\sigma_{13})^2 + N(\sigma_{12})^2]}, \quad (6)$$

with

$$\sigma_{11b} = \sigma_{11} - b_{11}; \quad \sigma_{22b} = \sigma_{22} - b_{22}; \quad \sigma_{33b} = \sigma_{33} - b_{33}, \quad (7)$$

The Hill parameters (F, G, H, L, M, N) would have to be identified from experiments.

The proposed anisotropic model provides a flexible general model for representation of the yield behaviour of the electrode particles and separator materials on a meso-modelling scale. However, identification of all material parameters would require extensive testing, which is not scope of the present macro-mechanical study. For the subsequent analysis, the general model is significantly simplified. Due to the assumption of isotropy, the Hill parameters are set to their isotropic values, $F = G = H = 0.5$, and $L = M = N = 1.5$, and the back stress vector is $\mathbf{b} = \mathbf{0}$. No data was available for the determination of a potential yield strength difference, hence $\alpha = 1$. So eventually, the yield criterion, equation (3), for the present macro-mechanical isotropic modelling approach is simplified to standard J_2 (von Mises) theory,

$$\bar{\sigma} = \sqrt{\frac{1}{2} \{ (\sigma_{11} - \sigma_{22})^2 + (\sigma_{11} - \sigma_{33})^2 + (\sigma_{22} - \sigma_{33})^2 + 6 [(\sigma_{23})^2 + (\sigma_{13})^2 + (\sigma_{12})^2] \}}. \quad (8)$$

A non-associated pressure dependent flow rule is proposed,

$$\Delta \boldsymbol{\varepsilon}^p = \Delta \lambda \frac{\partial \mathbf{g}}{\partial \boldsymbol{\sigma}}, \quad (9)$$

where $\Delta \boldsymbol{\varepsilon}^p$ is the plastic strain increment vector, $\Delta \lambda$ is the plastic multiplier, and \mathbf{g} is the flow rule function,

$$\mathbf{g} = \sqrt{\bar{\sigma}_{\text{dev}}^2 + \beta^2 \sigma_m^2}. \quad (10)$$

Shape parameter β can be related to the plastic Poisson ratio ν^p under uniaxial tension,

$$\beta = \frac{3}{\sqrt{2}} \sqrt{\frac{1 - 2\nu^p}{1 + \nu^p}}. \quad (11)$$

3.4. Parameter identification for the jelly roll, and simulation of the cell tests

The radial crushing load case is used for calibration of the plasticity model. CT analysis revealed that whilst the jelly roll becomes significantly compacted during the test, it exhibited almost no axial straining. The distance from the jelly roll to the boundary of the housing remained roughly the same, Fig. 10a. That is, the jelly roll exhibits almost perfect compressibility, which

corresponds to a low plastic Poisson's ratio in the material model. A non-zero value of $\nu^p = 0.15$ is used for numerical stability in the simulation model.

For the investigated load cases, the jelly roll deformation occurs mainly in radial compression and in radial shear direction. Considering the underlying monotonic mechanical loading, the differentiation of elastic and plastic strains is not necessary, but for the elasto-plastic constitutive model featuring additive strain decomposition, the elastic properties have to be input separately. Due to the relatively large Young's modulus of the current collector foils, the jelly roll deformation is mainly taking place in the non-metallic porous particle coatings of the jelly roll. Hence, a small Young's modulus is chosen for the jelly roll, using $E_{\text{jellyroll}} = 1.5$ GPa, which is calibrated along with the plastic strain hardening curve, for which the following analytical function is proposed:

$$R(\bar{\varepsilon}^p) = \left[\sigma_{\text{plateau}} - (\sigma_{\text{plateau}} - \sigma_{\text{yield}}) \times \text{Exp} \left(-\frac{\bar{\varepsilon}^p}{\bar{\varepsilon}_{\text{ref}}^p} \right) \right] \times [1 + s(\bar{\varepsilon}^p)^m]. \quad (12)$$

The first term represents the first phase of the hardening behaviour, from initial yield σ_{yield} , up to the intermediate plateau stress, σ_{plateau} , where $\bar{\varepsilon}_{\text{ref}}^p$ shapes the curvature of the hardening curve in between. The second term represents subsequent progressive strain hardening, controlled by the power law parameters s and m . The calibrated parameters are $\sigma_{\text{yield}} = 0.0003$ GPa, $\sigma_{\text{plateau}} = 0.0006$ GPa, $\bar{\varepsilon}_{\text{ref}}^p = 0.009$, $s = 1000$ and $m = 2.7$.

For the load case "radial crushing" the computed cell deformation is provided in Fig. 10b, being in good agreement with the experiment. The comparison of the load–displacement curves is provided in Fig. 11a, accompanied with the predicted load–displacement curves for the load cases "bending" (Fig. 11b) and "indentation" (Fig. 11c). All simulation curves are in good agreement with the corresponding experiment.

3.5. Development of a fracture and short circuit criterion for the jelly roll

As discussed in Section 2.2, macro-mechanical fracture of the jelly roll is clearly revealed from the CT analysis for the load case "bending", and also indicated by a significant sudden decrease of the punch force followed by the initiation of an internal short circuit for the load case "indentation", Fig. 3. It is assumed that fracture of the jelly roll leads to internal short circuit in all investigated load cases, since once fracture is initiated, the relative movement of the separated jelly roll parts easily leads to a short circuit initiating connection of anode and cathode material.

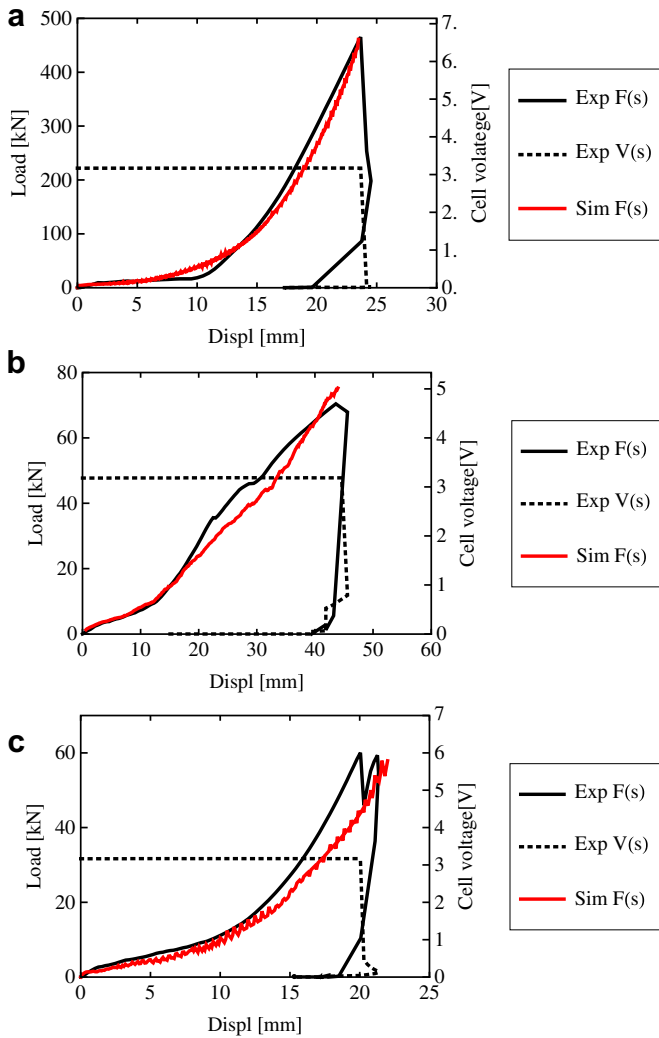


Fig. 11. Comparison of experimental and computed load–displacement curves, and the recorded voltage–displacement for the different load cases: a) “radial crushing”; b) “bending”; c) “indentation”.

In the fracture zone, the jelly roll is subject to compression–shear loading for the load cases “radial crushing” and “indentation” and subject to tensile loading for the load case “bending”. Hence, a fracture criterion is sought, which can take into account potential differences in the fracture behaviour under compressive/shear and normal stresses. The classical stress-based fracture criterion by Coulomb [19] and Mohr [20] can describe such

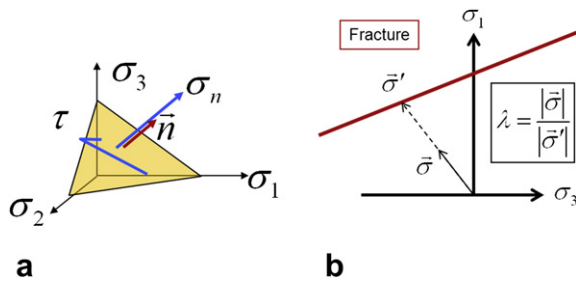


Fig. 12. Mohr–Coulomb fracture criterion: a) shear and normal stress acting on an arbitrary plane in principal stress space; b) graphical visualization of the solved maximum value problem in principal stress space, and the definition of scaling distance λ .

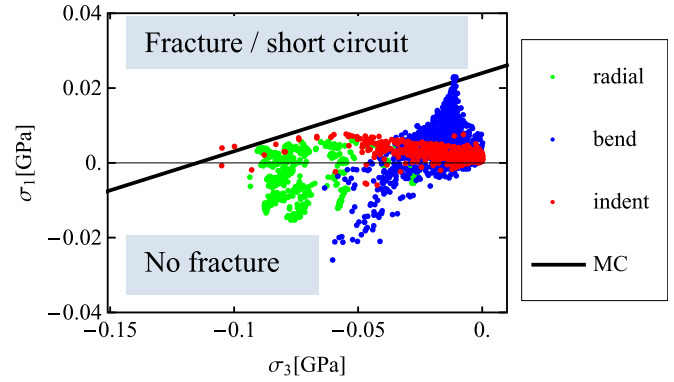


Fig. 13. Calibration procedure for the MC fracture/short circuit criterion.

behaviour. Hence, the criterion is reviewed and applied subsequently. The Mohr–Coulomb (MC) criterion for an isotropic continuum reads

$$\max\{\tau + c_1\sigma_n\} = c_2, \quad (13)$$

where τ and σ_n are the shear and normal stresses acting on a cutting plane in principal stress space, Fig. 12a. Fracture occurs on the plane perpendicular to the normal vector \vec{n} , where the shear stress τ plus the normal stress σ_n scaled by c_1 represents the maximum c_2 . In equation (13), c_1 and c_2 are material constants, which have to be calibrated from experiments.

The maximum value problem can be solved analytically, which has been done by Bai and Wierzbicki [21], for instance, leading to the simple expression

$$\sigma_1 = p\sigma_3 + 2c_2, \quad (14)$$

where σ_1 and σ_3 are the first and third principal stresses, respectively, and

$$p = \frac{(\sqrt{1 + c_1^2} - c_1)}{(\sqrt{1 + c_1^2} + c_1)}. \quad (15)$$

Equation (15) represents the fracture line, where fracture occurs once the combination of first and third principal stresses exceeds the line, Fig. 12b. For the simulation model, a scaling distance λ is introduced,

$$\lambda = \frac{|\vec{\sigma}|}{|\vec{\sigma}'|}, \quad (16)$$

which represents the scaling distance from the current stress state $\vec{\sigma}$, to the fracture (short circuit) line, $\vec{\sigma}'$, assuming a constant stress ratio, Fig. 12b. Jelly roll fracture, accompanied by an internal short circuit, occurs at $\lambda \geq 1$.

The calibration procedure for the MC model parameters c_1 and c_2 is as follows:

- Running the simulation models for all load cases to the punch displacement at which a short circuit is observed in the experiment.
- Visualize the final principal stresses (σ_1 and σ_3) of all finite elements of the jelly roll in one chart, Fig. 13.
- Determine the fracture line by calibrating the MC parameters (c_1 , c_2), Fig. 13.

The obtained values are $c_1 = 0.865$ and $c_2 = 0.012$ GPa.

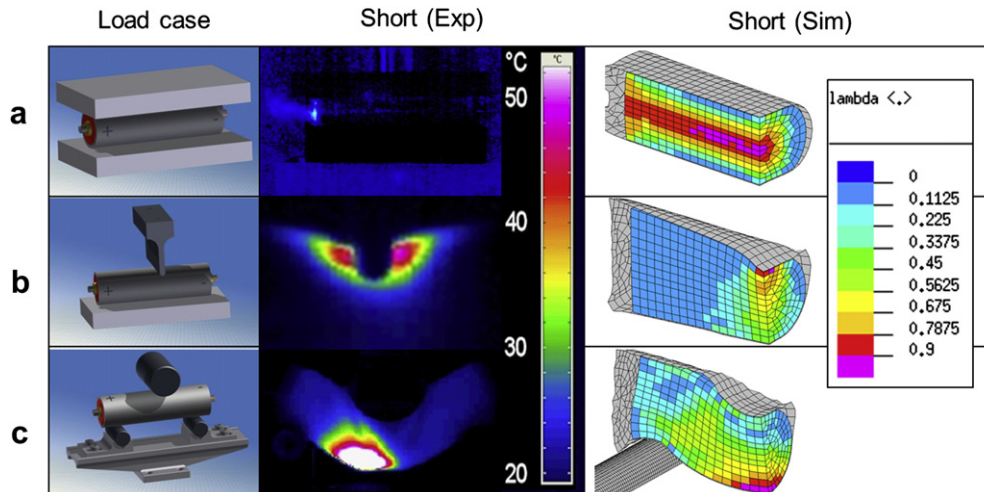


Fig. 14. Comparison of the experimentally observed short circuit locations and corresponding model predictions for the different load cases: a) “radial crushing”; b) “indentation”; c) “bending”.

It is noted that the calibration of the MC criterion is solely based on stress analysis, where the location of the short circuit was not taken into account by any means. Hence, it is now interesting to compare the predicted short circuit locations with the experimentally observed IR measurements provided in Fig. 14, in which high and highest temperatures are coloured red and white, respectively.

The experimental infrared picture of the load case “radial crushing”, Fig. 14a, indicates short circuit initiation at one end of the jelly roll, close to the pole connection. Examination of the longitudinal sectional plane of the corresponding simulation shown in Fig. 14a reveals that in the core zone of the jelly roll, the state of λ is quite homogeneous along the cell axis, and close to the limiting value of unity, at which fracture and internal short circuit is initiated. Therefore, it is assumed that the location of the short circuit initiation is eventually triggered by some mechanical interaction of the pole connector and the end of the jelly roll.

For the load case “indentation” the short circuit location is predicted close to the punch, whereas for the load case “bending” the location is predicted on the surface of the jelly roll opposite to the punch, Fig. 14b and c. Both predictions are in good agreement with the experimental observations, which indicates that the applied MC criterion provides a simple but useful method for the detection of jelly roll fracture and subsequent short circuit initiation.

4. Conclusions

A quasi-static mechanical test program on commercial cylindrical Lithium ion cells has been carried out, in order to assess the deformability until initiation of an internal short circuit. A macro-mechanical finite element model of the cell, suitable for standard crash simulations, has been set up, using an element mesh size of approximately 5 mm. The material model properties for the steel housing have been obtained from tensile tests, and the material properties for the jelly roll have been calibrated from one of the cell tests, namely the radial crushing load case. The classical stress-based fracture criterion after Mohr and Coulomb has been utilised for fracture modelling of the jelly roll, which is considered isotropic in the present study. It is shown that the Mohr–Coulomb criterion correctly predicts both the punch displacement to fracture, and also the correct different fracture locations for every load

case. The predicted fracture locations correspond to the observed locations of the internal short circuits of the cells. The testing demonstrated that the cells could withstand considerable deformation prior to the onset of an internal short circuit.

Future research should involve the experimental characterisation and numerical simulation of the individual jelly roll components (anode, separator and cathode) and their interaction during mechanical loading. Fracture analysis of the separator on a meso-scale could inspire the development of improved macro-scale models and criteria suitable for industrial applications.

Acknowledgements

The authors thank Dr. D.-Z. Sun from the Fraunhofer Institute for Mechanics of Materials IWM for valuable discussions, and Mr. Huberth and his co-workers from the Fraunhofer Ernst Mach Institute EMI in Freiburg for performing the CT analysis. Thanks are due to Dr. Bergmann, Dr. O. Nolte and Dr. F. Seyfried from VW Group Research for valuable discussions and partial financial support. The support of GAIA Akkumulatorenwerke GmbH is acknowledged.

References

- [1] BOOST – Transforming the Powertrain Value Chain, McKinsey, December 2012, online available at: <http://www.cars21.com/files/news/McKinsey%20-%20Boost!%20Transforming%20the%20powertrain%20value%20chain%20-%20a%20portfolio%20challenge.pdf>.
- [2] M. Yoshio, R.J. Brodd, A. Kozawa, Lithium-ion Batteries: Science and Technologies, Springer Science+Business Media, LLC, New York, 2009.
- [3] K.E. Aifantis, S.A. Hackney, R.V. Kumar, High Energy Density Lithium Batteries: Materials, Engineering, Applications, Wiley-VCH, Weinheim, 2010.
- [4] G. Venugopal, J. Moore, J. Howard, S. Pandalwar, Journal of Power Sources 77 (1999) 34–41.
- [5] S.S. Zhang, Journal of Power Sources 164 (2007) 351–364. doi:10.1016/j.jpowsour.2006.10.065 ISSN 0378-7753.
- [6] T.-H. Cho, M. Tanaka, H. Ohnishi, Y. Kondo, M. Yoshikazu, T. Nakamura, T. Sakai, Journal of Power Sources 195 (2010) 4272–4277.
- [7] X. Xiao, W. Wu, X. Huang, Journal of Power Sources 195 (2010) 7649–7660 ISSN 0378-7753.
- [8] X. Zhang, W. Shyy, A.M. Sastry, Journal of the Electrochemical Society 154 (2007) A910–A916.
- [9] R. Spotnitz, J. Franklin, Journal of Power Sources 113 (2003) 81–100. doi:10.1016/S0378-7753(02)00488-3 ISSN 0378-7753.
- [10] H. Maleki, J.N. Howard, Journal of Power Sources 191 (2009) 568–574.
- [11] R.M. Spotnitz, J. Weaver, G. Yeduvaka, D.H. Doughty, E.P. Roth, Journal of Power Sources 163 (2007) 1080–1086 ISSN 0378-7753.
- [12] M.D. Farrington, Journal of Power Sources 96 (2001) 260–265. doi:10.1016/S0378-7753(01)00565-1 ISSN 0378-7753.

- [13] E. Sahraei, R. Hill, T. Wierzbicki, *Journal of Power Sources* 201 (2012) 307–321.
- [14] E. Sahraei, R. Hill, T. Wierzbicki, Modeling of Lithium-ion Cylindrical Batteries for Mechanical Integrity: Experiments, Calibrations, and Validation, Battery Congress, Ann Arbor MI, April 2011.
- [15] Handhabungshinweise für die Lithium Ionen Zelle Typ HP 602030 NCA-45 Ah/162 Wh, online available at: http://www.gaia-akku.com/fileadmin/user_upload/downloads/Handhabungshinweis_HP602030NCA-45Ah.162Wh.pdf.
- [16] R. Hill, *Proceedings of the Royal Society of London* A193 (1948) 281–297.
- [17] H.W. Swift, *Journal of the Mechanics and Physics of Solids* 1 (1952) 1–76.
- [18] R. Raghava, R.M. Caddell, *Journal of Materials Science* 8 (1973) 225–232.
- [19] C.A. Coulomb, Essai sur une Application des Regles de Maximis et Minimis a Quelques Problèmes de Statique, Relatifs a l'Architecture, *Memoires de Mathematique et de Physique, Présentés, à l'Academie Royale des Sciences, Paris*, 7 (1776) 343–382.
- [20] O. Mohr, *Abhandlungen aus dem Gebiete der Technischen Mechanik*, second ed., Ernst, Berlin, 1914.
- [21] Y. Bai, T. Wierzbicki, *International Journal of Fracture* 169 (2010) 1–20.